

Article

Natural Sunlight Driven Photocatalytic Removal of Toxic Textile Dyes in Water Using B-Doped ZnO/TiO₂ Nanocomposites

Romana Akter Shathy¹, Shahriar Atik Fahim¹, Mithun Sarker¹ , Md. Saiful Quddus² ,
Mohammad Moniruzzaman³, Shah Md. Masum^{1,*} and Md. Ashraful Islam Molla^{1,*} 

¹ Department of Applied Chemistry and Chemical Engineering, Faculty of Engineering and Technology, University of Dhaka, Dhaka 1000, Bangladesh; s-2013912615@acce.du.ac.bd (R.A.S.); s-2015216823@acce.du.ac.bd (S.A.F.); mithun@du.ac.bd (M.S.)

² Institute of Glass and Ceramic Research and Testing, Bangladesh Council of Scientific and Industrial Research, Dhaka 1205, Bangladesh; mdsaifulquddus@gmail.com

³ Central Analytical and Research Facilities, Bangladesh Council of Scientific and Industrial Research, Dhaka 1205, Bangladesh; monirbcsir@gmail.com

* Correspondence: masumacce@du.ac.bd (S.M.M.); ashraful.acce@du.ac.bd (M.A.I.M.);
Tel.: +88-017-4946-7276 (S.M.M.); +88-015-5235-9706 (M.A.I.M.)

Abstract: A novel B-doped ZnO/TiO₂ (B-ZnO/TiO₂) nanocomposite photocatalyst was prepared using a mechanochemical–calcination method. For the characterization of the synthesized B-ZnO/TiO₂ photocatalyst, XRD, FESEM-EDS, FTIR, UV-Vis DRS, BET, PL, and XPS techniques were used. The bandgap energy of B-ZnO/TiO₂ was reduced, resulting in enhanced visible-light absorption. Significant PL quenching confirmed the reduction in the electron–hole recombination rate. Furthermore, reduced crystallite size and a larger surface area were obtained. Hence, the B-ZnO/TiO₂ photocatalyst exhibited better photocatalytic activity than commercial TiO₂, ZnO, B-ZnO, and ZnO/TiO₂ in the removal of methylene blue (MB) dye under natural sunlight irradiation. The effects of various parameters, such as initial concentration, photocatalyst amount, solution pH, and irradiation time, were studied. Under optimal conditions (MB concentration of 15 mg/L, pH 11, B-ZnO/TiO₂ amount of 30 mg, and 15 min of operation), a maximum MB removal efficiency of ~95% was obtained. A plausible photocatalytic degradation mechanism of MB with B-ZnO/TiO₂ was estimated from the scavenger test, and it was observed that the •O₂⁻ and •OH radicals were potential active species for the MB degradation. Cyclic experiments indicated the high stability and reusability of B-ZnO/TiO₂, which confirmed that it can be an economical and environmentally friendly photocatalyst.

Keywords: B-ZnO/TiO₂; photocatalyst; nanocomposite; mechanochemical; methylene blue; sunlight



Citation: Shathy, R.A.; Fahim, S.A.; Sarker, M.; Quddus, M.S.; Moniruzzaman, M.; Masum, S.M.; Molla, M.A.I. Natural Sunlight Driven Photocatalytic Removal of Toxic Textile Dyes in Water Using B-Doped ZnO/TiO₂ Nanocomposites. *Catalysts* **2022**, *12*, 308. <https://doi.org/10.3390/catal12030308>

Academic Editor: Vincenzo Vaiano

Received: 29 January 2022

Accepted: 3 March 2022

Published: 9 March 2022

Publisher's Note: MDPI stays neutral with regard to jurisdictional claims in published maps and institutional affiliations.



Copyright: © 2022 by the authors. Licensee MDPI, Basel, Switzerland. This article is an open access article distributed under the terms and conditions of the Creative Commons Attribution (CC BY) license (<https://creativecommons.org/licenses/by/4.0/>).

1. Introduction

Synthetic dyes are employed extensively in a variety of industries, including textiles, leather, cosmetics, and paint industries. Each year, over 0.8 million tons of different types of dyes are produced worldwide [1]. Approximately 15% of the world's total dye production is discarded and discharged in textile effluents [1,2]. The transfer of these colored waste streams into the ecosystem without proper treatment harms the environment and marine life and poses serious health threats to humans as they are toxic, recalcitrant, mutagenic, and carcinogenic [1]. For instance, methylene blue (MB, a thiazine cationic dye) has adverse health effects, which include breathing difficulties, vomiting, eye burns, diarrhea, and nausea when MB is accumulated in wastewater. In addition, due to its nonbiodegradability, it is highly persistent in the environment [1]. There are different conventional methods for the treatment of textile dyes in water, such as physical methods, biological methods, chemical precipitation, membrane filtration, reverse osmosis, ozonation, filtration, adsorption, ultrasonic-assisted adsorption, incineration, and coagulation [1,3–5].

Each treatment method, however, has certain drawbacks, including high energy waste, high cost, and the generation of secondary pollutants. Traditional physical methods are nondestructive, but instead of eradicating pollutants, they only transfer pollutants to other media, generating secondary pollution [4,6]. Even though biological methods are commonly used commercially, they still require the wastewater effluent to be diluted, as microalgae are susceptible to concentrated toxicity [3].

Advanced oxidation processes (AOP), particularly heterogeneous photocatalysis, have recently emerged as a potential destructive method for the total mineralization of most organic contaminants. Photocatalysis is a method that uses light as an energy source to activate a catalyst that speeds up chemical reactions without actually being consumed in the reaction. The photocatalytic reaction has several advantages, including the ability to occur at room temperature as well as almost complete mineralization of organic pollutants into CO_2 , H_2O , and N_2 . As a semiconductor photocatalyst, metal oxides such as ZnO, TiO_2 , ZrO_2 , SnO_2 , and WO_3 are employed [7]. Among these, ZnO and TiO_2 show similar properties. These include similar bandgap energy, better electro-optical properties, strong oxidation ability, high electron mobility, low toxicity, and an environmentally friendly nature [8,9]. In spite of having many favorable characteristics, there are still some drawbacks to ZnO and TiO_2 . Among the shortcomings, the most challenging ones for TiO_2 photocatalyst to overcome are (1) the large bandgap (ZnO = 3.37 eV and TiO_2 = 3.2 eV), which requires ultraviolet illumination [5,10], and (2) the high electron–hole pair recombination rate [5,7]. Additionally, in the presence of UV light, ZnO experiences photocorrosion problems as well as photoinstability and low quantum yield in aqueous solutions. Moreover, the most active phase of TiO_2 , i.e., anatase, is thermally unstable [7]. To overcome these shortcomings, a variety of techniques have been employed on ZnO and TiO_2 . These include metal and nonmetal doping, noble metal loading, dye sensitization, and semiconductor coupling [11–16]. Panwar et al. [17] fabricated Gd–ZnO/ TiO_2 nanocomposites via the sol–gel method and studied the photocatalytic degradation of organic dyes under UV irradiation. Kerli et al. [18] employed a hydrothermal method to synthesize Ag–ZnO/ TiO_2 nanocomposite particles for photocatalytic dye degradation. Li et al. [19] synthesized ZnO/ TiO_2 –B composite photocatalyst through a sol–gel method and evaluated the photodegradation of 4-chlorophenol under visible light irradiation. Wang et al. [20] used a microwave hydrothermal technique to produce C–ZnO/ TiO_2 composites and investigated the photocatalytic degradation efficiency of RhB under simulated sunlight irradiation.

The use of semiconductor coupling to enhance photocatalytic activity is a promising approach. Semiconductor coupling has been discovered to facilitate charge separation and inhibit electron–hole recombination [21,22]. This also provides additional benefits of increased charge transfer to adsorbed substrates, enhanced electro-optical properties, enhanced transport properties, and increased charge carrier period [7,19]. Moreover, the ionic radii of Zn^{2+} (0.74) and Ti^{4+} (0.75) are very close, which offers great potential for improving photocatalytic activity by semiconductor coupling of ZnO and TiO_2 . Furthermore, nonmetals such as B, C, F, N, S, and others are now being employed to reduce electron–hole recombination, enhance grain size, and increase surface area [23]. Because of the atomic size and electronic structure of B, B doping has attracted much attention [24]. In addition, the introduction of B inhibits the crystal growth, allowing a photocatalyst with a higher surface area to be achieved [9]. In view of these advantages, B and ZnO/ TiO_2 could be combined to yield extraordinary nanocomposites to achieve better photocatalytic activity. However, to the best of our knowledge, reports on the synthesis of B–ZnO/ TiO_2 nanocomposites using a simple mechanochemical–calcination method are scarce.

In this study, we synthesized B–ZnO/ TiO_2 nanocomposites and applied them for the removal of methylene blue (MB) dye from water. The effects of several parameters, such as photocatalyst amount, initial dye concentration, pH, and irradiation time, were investigated. Finally, the photocatalytic mechanism of the prepared nanocomposite photocatalyst was suggested on the basis of the radical-quenching experiments. This study's B–ZnO/ TiO_2 nanocomposites showed the rapid removal of MB (~95% within 15 min) from water, which

is considered a major breakthrough. Such a fast removal certainly strengthens the industrial application of the material for toxic dye removal from industrial effluents. The stability of the B-ZnO/TiO₂ was also confirmed for use in environmental purification.

2. Results and Discussion

2.1. XRD Study

This XRD analysis of commercial TiO₂, ZnO, B-ZnO, ZnO/TiO₂, and B-ZnO/TiO₂ nanoparticles is shown in Figure 1. According to Figure 1, there are diffraction peaks at $2\theta = 25.3^\circ, 36.9^\circ, 37.8^\circ, 38.6^\circ, 48.1^\circ, 53.9^\circ, 55.1^\circ, 62.1^\circ, 62.7^\circ,$ and 68.8° with corresponding planes (101), (103), (004), (112), (200), (105), (211), (213), (204), and (116), respectively, which are associated with anatase phases of TiO₂ (JSPDS No. 21-1272) [25]. The distinct peaks obtained for ZnO at $2\theta = 31.8^\circ, 34.4^\circ, 36.3^\circ, 47.5^\circ, 56.6^\circ, 62.9^\circ, 66.4^\circ, 68^\circ$ and 69.1° correspond to the planes (100), (002), (101), (102), (110), (103), (200), (112), and (201), respectively (JSPDS No. 36-1451) [23,26]. The Scherrer equation, $D = 0.9\lambda/\beta\cos\theta$, was used to calculate the crystallite sizes of TiO₂, ZnO, B-ZnO, ZnO/TiO₂, and B-ZnO/TiO₂ from the full width at half maximum (FWHM) of the corresponding crystal peaks, as shown in Table 1. Here, D is the average crystallite size, λ is the X-ray wavelength, θ is the Bragg diffraction angle, and β is the full width at half maximum. Additionally, peaks observed for B-ZnO/TiO₂ were found to have both peaks associated with ZnO and TiO₂ combined, and the intensity for selective peaks was decreased compared with pristine TiO₂ and ZnO, which indicates a smaller crystallite size formed, providing enhanced photodegradation efficiency [23].

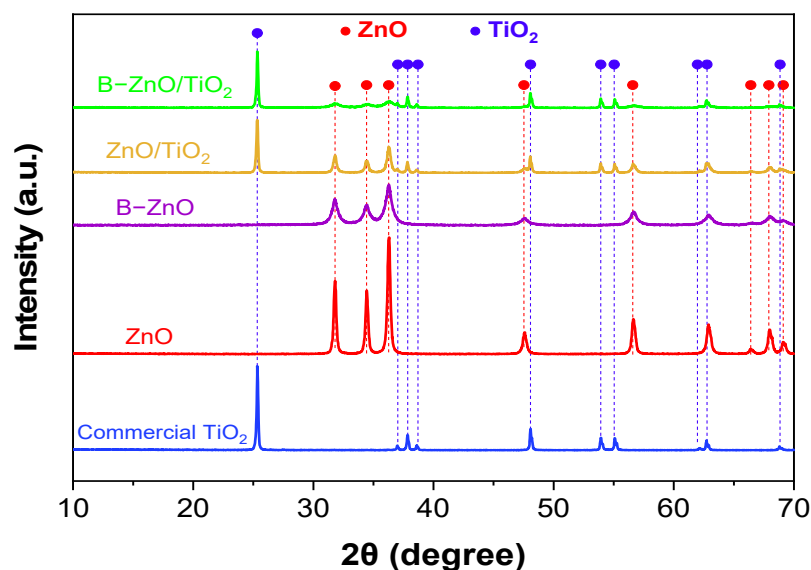


Figure 1. XRD diffraction patterns of TiO₂, ZnO, B-ZnO, ZnO/TiO₂, and B-ZnO/TiO₂.

Table 1. Crystallite size, BET parameters, and bandgap energies.

Photocatalysts	Crystallite Size (nm)	BET Parameters		Bandgap Energies (eV)	
		BET Surface Area (m ² /g)	Pore Volume (cm ³ /g)	Direct Transitions	Indirect Transitions
Commercial TiO ₂	73.35	10.76	0.0371	—	3.21
ZnO	32.10	7.30	0.0732	3.22	—
B-ZnO	14.03	—	—	3.18	—
ZnO/TiO ₂	52.40	—	—	2.93	3.13
B-ZnO/TiO ₂	42.54	18.99	0.0781	2.89	3.06

2.2. FESEM Study

The surface, size, and particle morphologies of the commercial TiO_2 , synthesized ZnO, B-ZnO, ZnO/ TiO_2 , and B-ZnO/ TiO_2 photocatalysts evaluated by FESEM are visualized in Figure 2. In Figure 2a, TiO_2 shows globular-shaped fine nanoparticles with a homogeneous distribution, as described in the literature [27]. The micrograph of ZnO reveals its morphological appearance is polycrystalline in nature. Most of the particles possess smooth surfaces and are polygonal in shape, which indicates that the samples were polycrystalline wurtzite structure, as presented in Figure 2b [28]. Images of B-ZnO are of irregular spheroid structure structures with a greater extent of agglomeration (Figure 2c). Particle size was also reduced after the incorporation of boron (B) into ZnO, which indicates successful doping [23]. As shown in Figure 2d, by incorporating ZnO into TiO_2 , the observed morphology seems to retain properties of both ZnO and TiO_2 with a higher degree of agglomeration. The micrograph of B-ZnO/ TiO_2 demonstrates smaller spherical-shaped particles with less agglomeration compared to both ZnO and TiO_2 (Figure 2e,f). Generally, B doping deteriorates the crystallinity of ZnO to a certain extent [29], because the radius of B^{3+} (0.02 nm) is smaller than that of O^{2-} (0.14 nm) and Zn^{2+} (0.074 nm). As a result, when the O or Zn atoms are replaced with B, the crystal plane spacing shrinks, causing the diffraction peaks to shift to a greater angle. Consequently, the B atoms are likely to occupy the octahedral interstices [29]. However, Figure 2e exhibited substantially larger particles because the FESEM image of the heterogeneous semiconductor photocatalyst B-ZnO/ TiO_2 was focused where TiO_2 nanoparticles were more predominant. To make it easier to understand, another FESEM picture of B-ZnO/ TiO_2 nanocomposites has been presented (Figure 2f), which shows characteristics of both B-ZnO and TiO_2 .

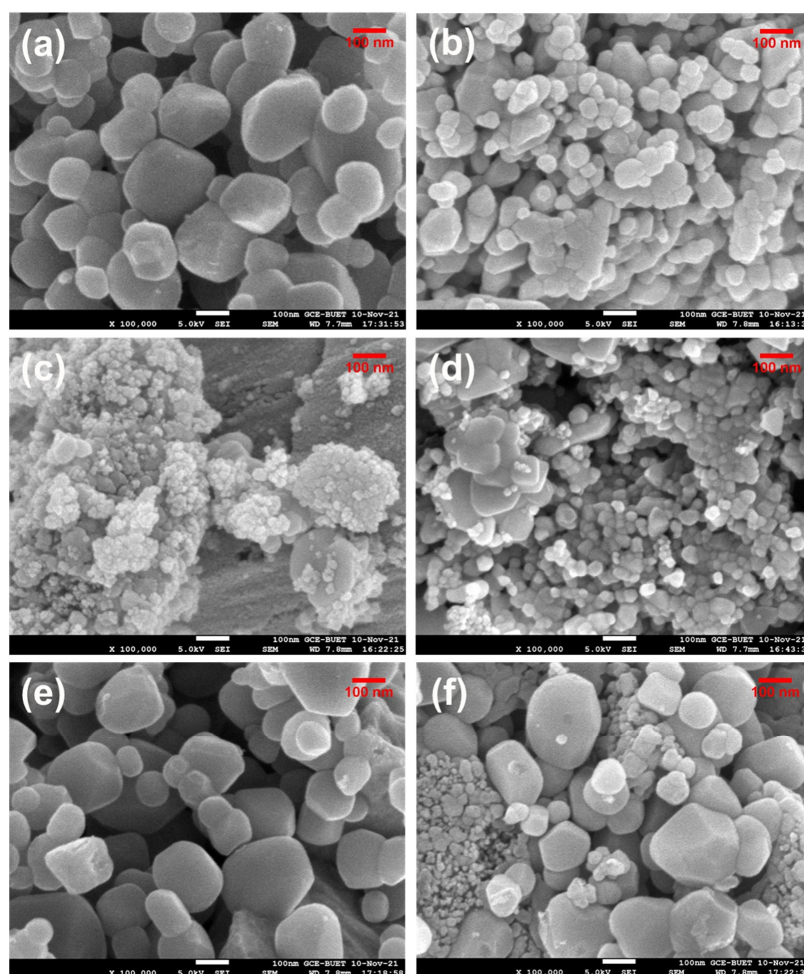


Figure 2. FESEM images of (a) TiO_2 , (b) ZnO, (c) B-ZnO, (d) ZnO/ TiO_2 , and (e,f) B-ZnO/ TiO_2 .

The calculations for average particle size of nanocomposites were carried out through ImageJ software. The nanoparticles were marked at 59 different locations for TiO₂, 132 for ZnO, and 61 for B-ZnO/TiO₂ using Figure 2a, Figure 2b, and Figure 2e, respectively, and plotted as a size distribution histogram (Figure S1a–c). The average particle size of nanocomposites is calculated to be 114, 53, and 88 nm for TiO₂, ZnO, and B-ZnO/TiO₂ respectively. The average particle size measured by FESEM shows a good agreement with the XRD.

2.3. SEM and EDS Mapping Study

SEM and EDS mapping examinations were carried out on synthesized B-ZnO/TiO₂ nanocomposite to determine the presence of boron (B) atom in the sample (Figure S2). From Figure S2b–e, it was observed that the various elements of B, Zn, Ti, and O were distributed throughout the sample, confirming the presence of all elements and the successful synthesis of B-ZnO/TiO₂ nanocomposites.

2.4. EDS Study

Figure S3 show the energy-dispersive X-ray spectroscopy (EDS) line-scanning outputs of commercial TiO₂, ZnO, B-ZnO, ZnO/TiO₂, and B-ZnO/TiO₂ photocatalysts. From the EDS spectrum of commercial TiO₂ (Figure S3a), sharp peaks of elemental Ti and O have been found. Figure S3b shows the strong peaks of elemental Zn and O in the EDS spectra of ZnO. Peaks related to elements B, Zn, and O are found in the EDS spectra of B-ZnO (Figure S3c). Figure (S3d) depicts EDS spectra of ZnO/TiO₂ with sharp peaks for the elements Zn, Ti, and O. From the EDS spectra analysis of B-ZnO/TiO₂ shown in Figure S3e, peaks related to elements of B, Zn, Ti, and O have been found, confirming the presence of all four elements. No other peaks of different elements were found, which confirms the formation of a pure B-ZnO/TiO₂ composite. The elemental mass percentage and atom percentage of all photocatalysts are presented in Table S1. From Table S1, the obtained values for mass percentage and atom percentage are very close to stoichiometric values. However, composites containing boron, namely B-ZnO and B-ZnO/TiO₂, show an exception. The amount of boron present in the photocatalysts could not be measured even though a peak of boron exists in the EDS spectra. This was due to the inability of the EDS instrument to detect elements with lower molecular weight [30]. However, when the mass percentage of B-ZnO was compared to ZnO and B-ZnO/TiO₂ was compared to ZnO/TiO₂, it was discovered that the mass percentage changed significantly with the increased amount of oxygen present in boron-doped composites. This ensures changes in composition with the incorporation of boron in B-ZnO and B-ZnO/TiO₂.

2.5. FTIR Study

Figure 3 illustrates the Fourier transform infrared spectroscopy (FTIR) results of commercial TiO₂, ZnO, B-ZnO, ZnO/TiO₂, and B-ZnO/TiO₂ photocatalysts. The FTIR spectrum of TiO₂ displays a broad band between 470 and 865 cm⁻¹ owing to the overlapping of several bands assigned to Ti–O–Ti and Ti–O vibration modes [31]. The intense peak near 675 cm⁻¹ is attributed to the Ti–O stretching [32]. The major characteristic peaks obtained for ZnO between 460 and 540 cm⁻¹ are because of the absorption band with the stretching mode of Zn–O [23,26]. The peaks observed between 1600 and 700 cm⁻¹ are responsible for the B–O stretching vibrations. This confirms the successful doping of boron into ZnO. The IR spectrum assigned to ZnO/TiO₂ illustrates the fingerprint region of both ZnO and TiO₂. Furthermore, B-ZnO/TiO₂ introduces a weak peak at 1300 cm⁻¹ associated with B–O stretching vibrations. The stretching and bending vibrations of H–O–H and O–H showed signals in the ranges of 3000–3800 cm⁻¹ and 1600–1650 cm⁻¹. From the intensity of these peaks, it can be affirmed that the moisture content of all photocatalysts is negligible. No other peaks are found in the IR spectra. Therefore, each photocatalyst is free of any type of contamination, which is consistent with the EDS results.

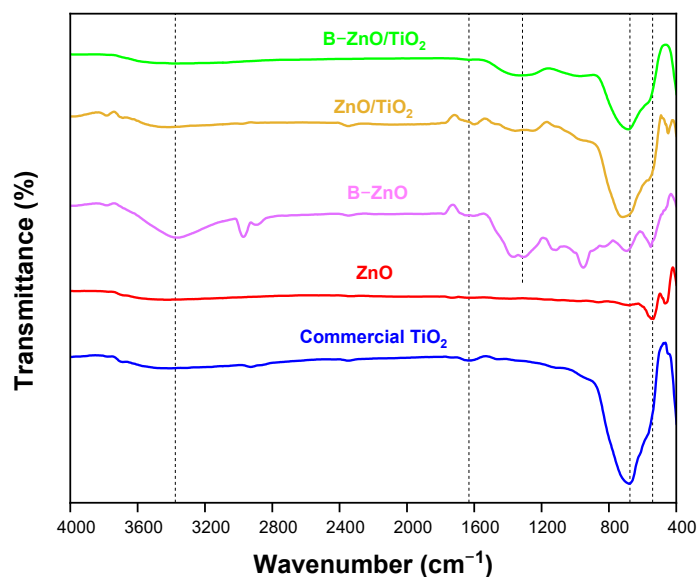


Figure 3. FTIR spectra of TiO_2 , ZnO, B-ZnO, ZnO/ TiO_2 , and B-ZnO/ TiO_2 .

2.6. UV-Vis DRS Study

Figure 4a represents the diffuse reflectance spectra (DRS) measured from 300 nm to 700 nm. From the DRS, commercial TiO_2 , ZnO, B-ZnO, ZnO/ TiO_2 , and B-ZnO/ TiO_2 photocatalysts show optical absorption below 400 nm. The photocatalysts demonstrate high reflectance at visible wavelengths. A rapid rise in reflectance has been observed for TiO_2 , ZnO, B-ZnO, ZnO/ TiO_2 , and B-ZnO/ TiO_2 at the absorption edge at 414, 440, 430, 455, and 411 nm, respectively.

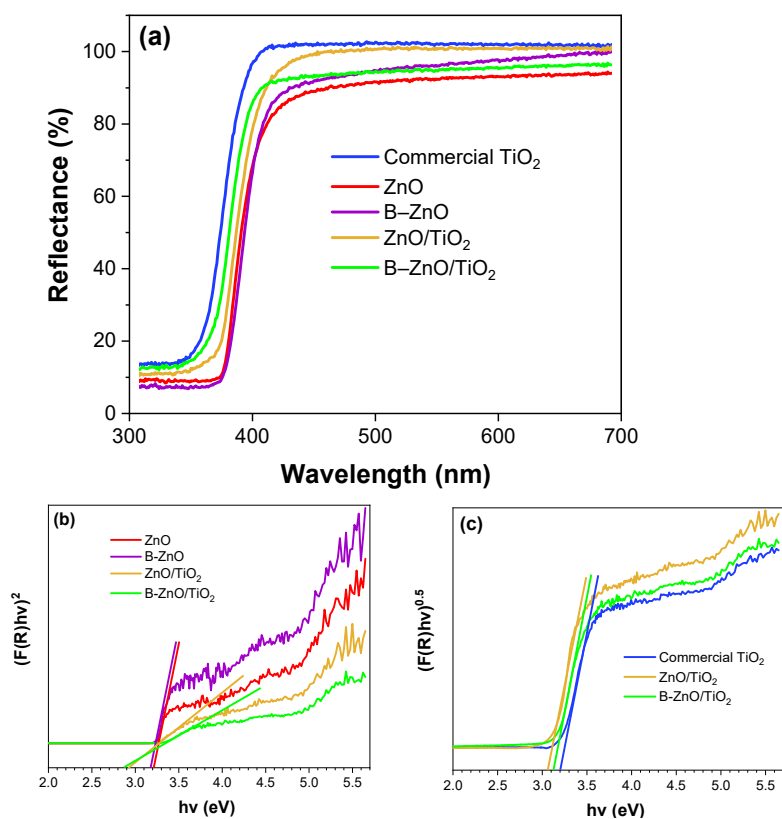


Figure 4. (a) UV-Vis DRS patterns of TiO_2 , ZnO, B-ZnO, ZnO/ TiO_2 , and B-ZnO/ TiO_2 ; Tauc plot for (b) direct and (c) indirect transitions.

The Kubelka–Munk function given by Equation (1) has been used to calculate the bandgap E_g , where equivalent absorption coefficient is obtained from reflectance R .

$$F(R) = (1 - R)^2/2R \quad (1)$$

where $F(R)$ represents the Kubelka–Munk function and is proportional to the absorption coefficient α , and R is the reflectance. By extrapolating the straight portion of the plot of $(\alpha h\nu)^{1/n}$ versus $h\nu$ to the $h\nu$ axis of the Tauc equation, the bandgap of the photocatalyst can be determined.

$$F(R) \times h\nu = A (h\nu - E_g)^n \quad (2)$$

Here, A is the proportionality constant and h is Planck's constant ($6.63 \times 10^{-34} \text{ Js}^{-1}$). In this case, for direct allowed transitions, $n = 1/2$, and for indirect transitions, $n = 2$. Studies revealed that the direct bandgap is followed by ZnO and TiO₂ follows the indirect bandgap. So, both $n = 0.5$ and $n = 2$ were applied to the B–ZnO/TiO₂ photocatalysts to obtain a more accurate bandgap (Figure 4b,c) [33]. The estimated bandgap energies of photocatalysts TiO₂, ZnO, B–ZnO, ZnO/TiO₂, and B–ZnO/TiO₂ are presented in Table 1. The B–ZnO/TiO₂ photocatalyst exhibits a decrease in bandgap energy compared with TiO₂ and ZnO owing to the introduction of B–ZnO with TiO₂ [34]. The lowest values of bandgap are obtained for B–ZnO/TiO₂ (~ 2.89 eV for $n = 0.5$ and ~ 3.06 eV for $n = 2$). The electrons from the conduction band injected from ZnO to TiO₂ may be responsible for the bandgap narrowing. This is also favorable to electron–hole (e^-/h^+) separation and increased photocatalytic activity of B–ZnO/TiO₂. Moreover, the bandgap energies of B–ZnO/TiO₂ for both direct and indirect transitions are consistent with previously published literature [20].

2.7. BET Study

Figure 5 demonstrates N₂ adsorption/desorption isotherms of commercial TiO₂, ZnO, and B–ZnO/TiO₂ photocatalysts. According to the IUPAC classification, the adsorption/desorption isotherms are found to be of type IV. Table 1 summarizes the BET surface area of TiO₂, ZnO, and B–ZnO/TiO₂ photocatalysts. The BET surface areas of ZnO and TiO₂ are 7.30 and 10.76 m²/g, respectively, whereas B–ZnO/TiO₂ has a surface area of 18.99 m²/g, which is consistent with previous findings [35]. Interestingly, B–ZnO/TiO₂ exhibits a higher BET surface area than bare ZnO and TiO₂. The increase in surface area of B–ZnO/TiO₂ may be associated with the incorporation of boron, which prevents agglomeration of the ZnO and TiO₂ in the nanocomposite, and is also in agreement with FESEM analysis. As a result, the addition of boron increases the surface area and also increases the number of active sites. This suggests that the synergistic influence of adsorption and photocatalysis of B–ZnO/TiO₂ enables the removal of more MB dye molecules from water [36].

2.8. PL Study

Figure 6 presents the photoluminescence (PL) spectra of commercial TiO₂, ZnO, B–ZnO, ZnO/TiO₂, and B–ZnO/TiO₂ photocatalysts. The photocatalysts were all excited at 325 nm at room temperature. The PL spectrum of TiO₂ displays one significant peak at 376 nm, whereas ZnO shows a broad hump at 425–600 nm in the visible region. The broad hump near 553 nm corresponds to the oxygen vacancies, whereas the peak at 382.5 nm refers to the band edge emission [37,38]. The PL spectrum of B–ZnO/TiO₂ photocatalyst reveals a small band edge emission at 380 nm and a very weak peak in the visible region. Hence, the decay in the PL intensity suggests a decline in the recombination rate of photogenerated e^-/h^+ pairs of B–ZnO/TiO₂. Moreover, the PL intensity is weakened for B–ZnO compared with bare ZnO, suggesting an efficient electron capture by the doped B energy level [19]. Thus, combining B–ZnO with the TiO₂ nanoparticles enhanced the separation efficiency of e^-/h^+ in B–ZnO/TiO₂ which consequently improved the photocatalytic activity [39]. Moreover, the crystal quality can be evaluated using UV emission

luminescence, whilst the occurrence of structural defects can be detected using visible light emission. Relatively low photoluminescence intensity suggests a slow rate of electron–hole recombination, while a very large PL intensity indicates a fast rate of recombination. During the fast reaction formation process, surface and subsurface defects occurred, resulting in higher intensity. Furthermore, highly crystalline materials exhibit a higher PL peak intensity than amorphous materials [21].

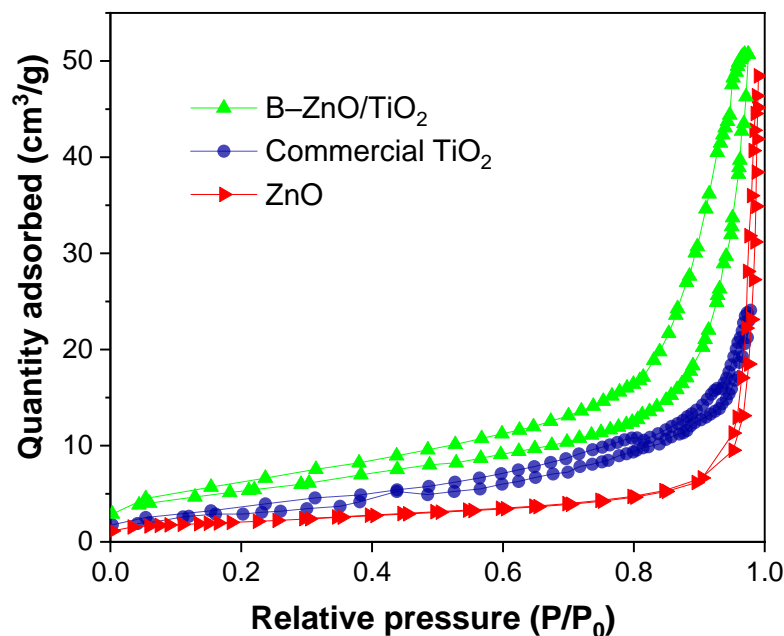


Figure 5. Nitrogen adsorption–desorption isotherms of TiO_2 , ZnO , and B-ZnO/TiO_2 .

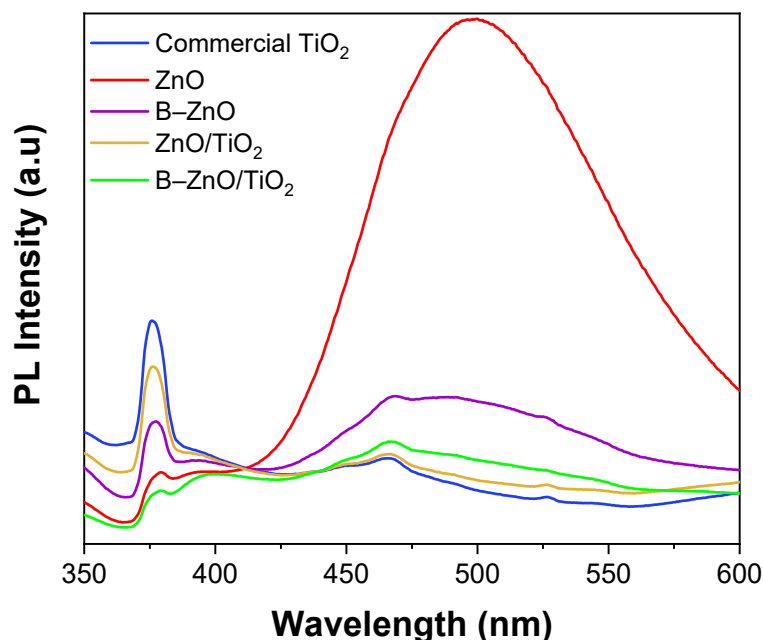


Figure 6. PL spectra of TiO_2 , ZnO , B-ZnO , ZnO/TiO_2 , and B-ZnO/TiO_2 .

2.9. XPS Study

X-ray photoelectron spectroscopy (XPS) was used to analyze the surface compositions and related valence states of the B-ZnO/TiO_2 photocatalyst. Figure 7a shows the XPS full survey spectrum, which clearly shows the peaks of Zn, Ti, B, O, and C elements. During

the synthesis process, the C ingredient could have come from hydrocarbons. As a result, the nanocomposites are only made up of Zn, Ti, B, and O, and these findings are consistent with the XRD patterns. The high-resolution spectra of Zn 2p are shown in Figure 7b. The Zn 2p_{3/2} and Zn 2p_{1/2} of Zn²⁺ are responsible for the peaks centered at 1022.2 and 1045.3 eV, respectively [23]. Figure 7c displays two peaks in the Ti 2p XPS spectrum, Ti 2p_{3/2} (458.6 eV) and Ti 2p_{1/2} (464.4 eV) [9,20]. Figure 7d shows the binding energy peak of B 1s at 192.3 eV, showing that the doping B atoms are in the trivalent state of B³⁺ [9,23]. Furthermore, the O 1s XPS spectra of B–ZnO/TiO₂ (Figure 7e) reveal that the peak at 529.9 eV is attributable to the lattice oxygen anions (O²⁻) [23,35]. The peak at 531.2 eV relates to weakly bound oxygen species such C–O and C=O groups, whereas the peak at 532.2 eV indicates the presence of OH groups on the nanocomposite surface [20,23].

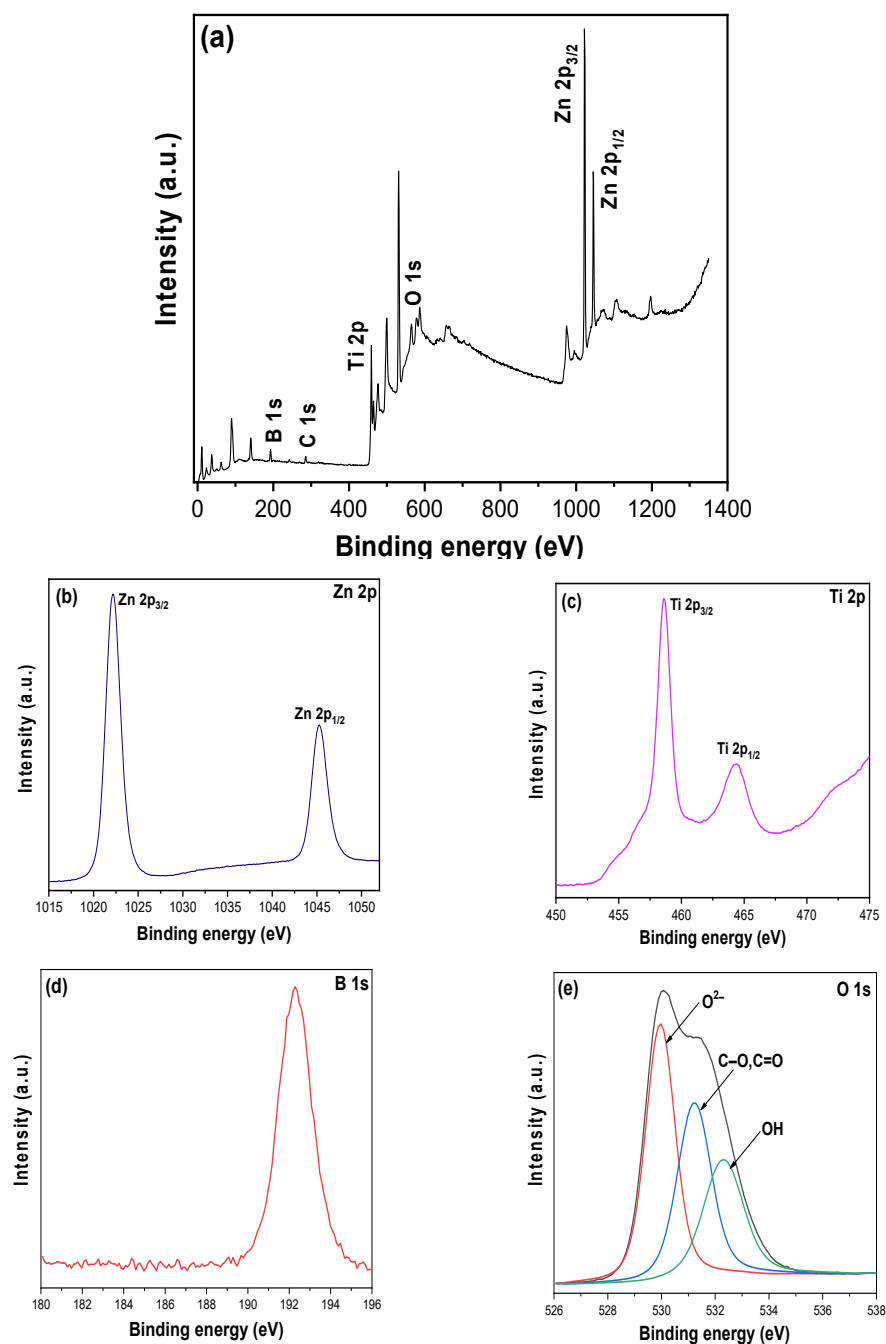


Figure 7. XPS spectra of B–ZnO/TiO₂ (a) survey, (b) Zn 2p, (c) Ti 2p, (d) B 1s, and (e) O 1s.

2.10. Photocatalytic Removal of MB Dye

The UV–visible absorption spectra of MB dye with commercial TiO_2 , ZnO, B–ZnO, ZnO/ TiO_2 , and B–ZnO/ TiO_2 photocatalysts are illustrated in Figure 8a (natural pH 6) and Figure 8b (optimized pH 11). The intensity of the major peak of MB ($\lambda_{\text{max}} = 662 \text{ nm}$ [11]) decreases with various photocatalysts. The peak intensity decreases with reduced dye concentration due to the photocatalytic removal in the presence of photocatalysts and sunlight irradiation. Photolysis of MB at a natural pH of 6 and an optimized pH of 11 was performed for 15 min under sunlight without a photocatalyst to monitor self-degradation (Figure 8c). It is observed that the self-degradation of MB dye solution is negligible at both pH levels during the photocatalytic test [40]. Without sunlight irradiation, another set of experiments was conducted to determine the removal efficiency of MB in the dark because of the dye adsorption on the B–ZnO/ TiO_2 photocatalyst surface. In the dark, the removal efficiency of MB with B–ZnO/ TiO_2 is 10.52% and 48.58% at pH 6 and pH 11, respectively. At basic pH, B–ZnO/ TiO_2 showed greater dye removal efficiency. This can be explained as, at basic conditions, the positively charged cationic MB dye is easily absorbed on the strongly negatively charged photocatalyst surface.

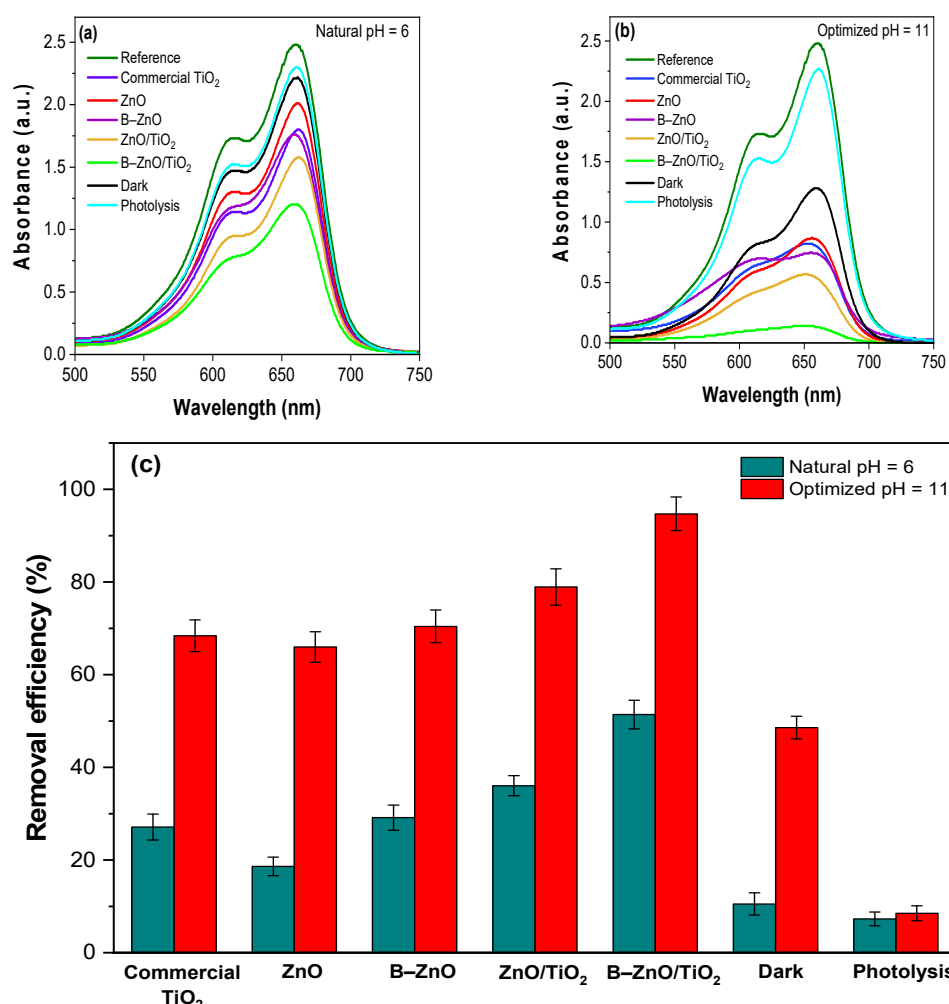


Figure 8. (a,b) UV–visible results showing the decay in the intensity of MB solution; (c) Photocatalytic removal, adsorption under dark, and photolysis for MB (initial MB concentration: 15 mg/L; photocatalyst amount: 30 mg; pH: 6 and 11; irradiation time: 15 min).

The understanding of the photocatalytic removal efficiency of synthesized photocatalysts is of great importance. A series of experiments were conducted with commercial TiO_2 , ZnO, B–ZnO, ZnO/ TiO_2 , and B–ZnO/ TiO_2 photocatalysts at natural pH 6 and opti-

mized pH 11 while keeping other parameters constant, as shown in Figure 8c. From the photocatalytic experiments, the MB removal efficiencies of commercial TiO₂, ZnO, B-ZnO, ZnO/TiO₂, and B-ZnO/TiO₂ were found to be 27.12%, 18.62%, 29.14%, 36.03%, and 51.41%, respectively, at the natural pH of dye (pH 6). The MB removal efficiencies at optimized pH 11 were found to be 68.42%, 65.99%, 70.44%, 78.94%, and 94.73%, respectively, after 15 min of irradiation. There is a significant rise in the MB removal efficiency of B-ZnO/TiO₂ compared with pristine TiO₂ and ZnO. It also exceeds B-ZnO and ZnO/TiO₂ by a sufficient amount. This can be explained as the coupling of TiO₂ with ZnO suppresses the e⁻/h⁺ recombination rate [40,41], which is consistent with the PL results. Moreover, boron doping can substantially inhibit crystal size growth [9,19], which is confirmed by XRD, hence increasing photocatalytic activity [9]. Furthermore, the surface area of B-ZnO/TiO₂ increases and the bandgap energy decreases for B-ZnO/TiO₂, as confirmed by BET and UV-Vis DRS data, respectively. Thus, B, ZnO, and TiO₂ altogether resulted in a synergistic effect to obtain enhanced photocatalytic performance of B-ZnO/TiO₂ [17,26]. Furthermore, B-ZnO/TiO₂ nanocomposites exhibit superior photocatalytic performance compared to other nanocomposites presented in the literature [17,18,20,40–45], as summarized in Table 2, indicating that B-ZnO/TiO₂ can be a promising photocatalyst for the removal of organic dyes.

Table 2. Comparison of the photocatalytic activity of B-ZnO/TiO₂ nanocomposites with recently reported doped ZnO/TiO₂ nanocomposites for organic dye removal.

Nanocomposites	Synthesis Methodology	Dye Concentration	Photocatalyst Dimension	Time (min)	Light Source	Removal Efficiency	Ref.
B-ZnO/TiO ₂	Mechanochemical-calcination method	MB (15 mg/L)	30 mg/50 mL	15	Natural sunlight (~1.2 mW/cm ²)	~95%	Presentstudy
Gd-ZnO/TiO ₂	Sol-gel method	MB (20 mg/L) MO (20 mg/L)	1 g/L	90	Fluorescent lamps (30 W)	93% (MB) 94% (MO)	[17]
Ag-ZnO/TiO ₂	Hydrothermal method	MB, RhB, MG (5 mg/L)	10 mg/50 mL	120	Xenon lamp (300 W)	99% (MB) 87% (RhB) 71% (MG)	[18]
C-ZnO/TiO ₂	Hydrothermal-calcination method	RhB (10 mg/L)	50 mg/100 mL	45	Xenon lamp (200 W)	94%	[20]
ZnO/TiO ₂ -CNFs	Hydrothermal method	MB (10 mg/L)	20 mg/25 mL	120	Ultraviolet lamp (λ = 365 nm)	93%	[40]
Cu-TiO ₂ /ZnO	Sol-gel method	MO MB	0.7 g/L	120	Fluorescent lamp (18–23 W)	85% (MO) 73% (MB)	[41]
S-ZnO/TiO ₂	Sol-gel method	RhB (2.5 × 10 ⁻⁵ mol/L)	50 mg/100 mL	100	Halogen lamps (125 W)	92%	[42]
Ni-ZnO/TiO ₂	Sol-gel method	RBB (50 mg/L)	1 g/L	120	Simulated sunlight (350 W Xe lamp)	61%	[43]
Au-ZnO/TiO ₂	Hydrothermal	MO (10 mg/L)	3.34 mg/50mL	300	Mercury lamp (300 W)	95%	[44]
ZnO/TiO ₂ -rGO	Solvothermal method	MB (20 mg/L)	252.5 mg/L	63.5	Ultraviolet lamp (11 W)	99%	[45]

2.11. Effect of pH

The pH of the reaction medium has a substantial impact on the photocatalytic performance of the catalyst. This is because the surface characteristics and the size of aggregated nanocomposites are influenced by pH. The pH can also influence the charge of dye molecules as well as the concentration of reactive hydroxyl radicals [5]. To understand the pH effect, experiments were conducted with the pH varying from 3 to 12 while the other parameters remained constant. Figure 9 represents the experimental outcomes. Overall, MB removal efficiency increases with increasing pH, and the maximum stands at the most basic pH 12, more than 98.32% degradation within 15 min. A rapid increasing trend is found from pH 3 to pH 10, with a removal efficiency of between 20.59% and 88.69%, and then it rises steadily. At pH 11, which is taken as the optimum pH, MB removal efficiency of 94.73% was obtained. Because textile waste effluent has a characteristic pH of 10 [46], pH 11 will be feasible and effective for almost complete removal of dye without introducing any additional pollution. The pH effect can be explained on the basis of electrostatic attraction between the photocatalyst and the dye. The photocatalyst's surface charge properties are influenced by the acidity or basicity of the solution, which has a direct impact on its photoactivity. The photocatalyst becomes less attracted to the dye molecules at zero charge point (pH_{PZC}). The literature reveals that pH_{PZC} is ~ 6.0 for TiO_2 [40,47] and ~ 9.0 for ZnO [40,48]. Therefore, the protonation reaction occurs at $\text{pH} < \text{pH}_{\text{PZC}}$, and the surface of the catalyst becomes positively charged. In contrast, the deprotonation reaction occurs at $\text{pH} > \text{pH}_{\text{PZC}}$, resulting in a negatively charged catalyst surface [5,40]. MB is a cationic dye with a pH of ~ 6 in solution [5]. At acidic pH, the positively charged B-ZnO/TiO₂ photocatalyst and the cationic MB dye are electrostatically repulsed, resulting in reduced photoactivity. On the other hand, at basic conditions, a strong electrostatic attraction facilitates the positively charged cationic dye MB to be adsorbed on the strongly negatively charged B-ZnO/TiO₂ surface. This electrostatic interaction facilitates the adsorptive property, which consequently enhances the photocatalytic removal efficiencies. These findings are completely consistent with previously published reports [40].

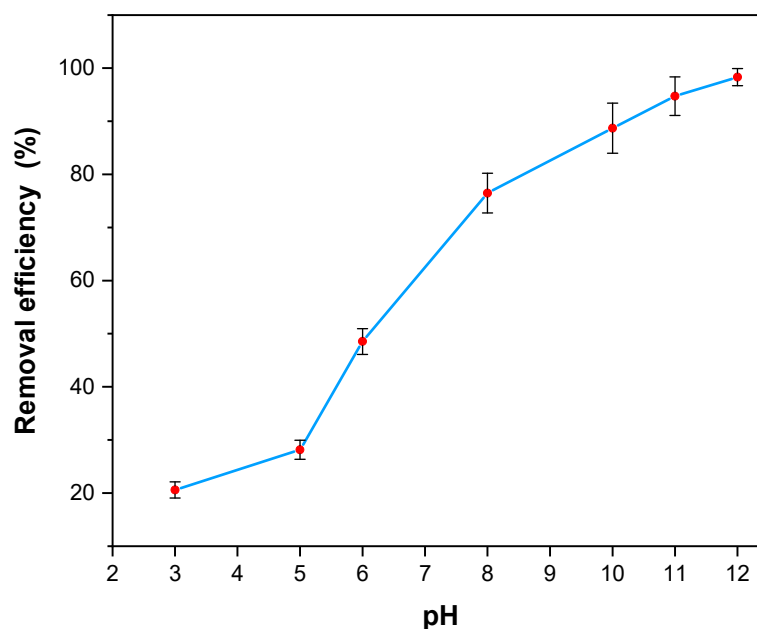


Figure 9. Effect of pH on the photocatalytic removal of MB with B-ZnO/TiO₂ (initial MB concentration: 15 mg/L; photocatalyst amount: 30 mg; pH: 3–12; irradiation time: 15 min).

2.12. Effect of Photocatalyst Dosages

The photocatalytic removal efficiency has a direct relation to the amount of photocatalyst used during the photodegradation process. This is due to the fact that the efficiency

of photocatalytic removal is dependent on the photon absorption capacity of the catalysts and the active site availability of the catalysts [9]. To investigate the effects of photocatalyst dosage on the photocatalytic removal of MB dye, experiments were conducted with the most active photocatalyst B-ZnO/TiO₂ by varying the amount, ranging from 10 to 50 mg (Figure 10). It is noticed that the MB removal efficiency increased linearly from 63.13% to 94.73% with the increase in photocatalyst loading from 10 to 30 mg. However, the removal efficiency declined to 83.13% and 73.19% on further loading of the photocatalyst up to 40 and 50 mg, respectively. This suggests that the MB degradation has a maximum dosage of 30 mg. The increase in removal efficiency with increasing catalyst loading can be explained as the availability of active sites in the photocatalyst is higher compared to the MB molecules present. At low photocatalyst dosages, the number of catalyst active sites is insufficient for higher amounts of dye molecules. As a result, only a limited number of active radicals are produced. With increased photocatalyst, the generation of active radicals, for example, superoxide and hydroxyl radicals, increases, resulting in more free electrons in the conduction band and higher light absorption. Therefore, the photocatalytic activity is significantly enhanced [7,9]. When the photocatalyst loading is very high, the catalyst may scatter light photons, and its turbidity may completely block UV light penetration. As a result, the photocatalytic removal efficiency is reduced. Another factor that contributes to low efficiency is the agglomeration of catalyst particles due to excess catalyst. As a result, the exposed surface area of the catalyst is reduced, and the catalyst becomes inactive [7,49].

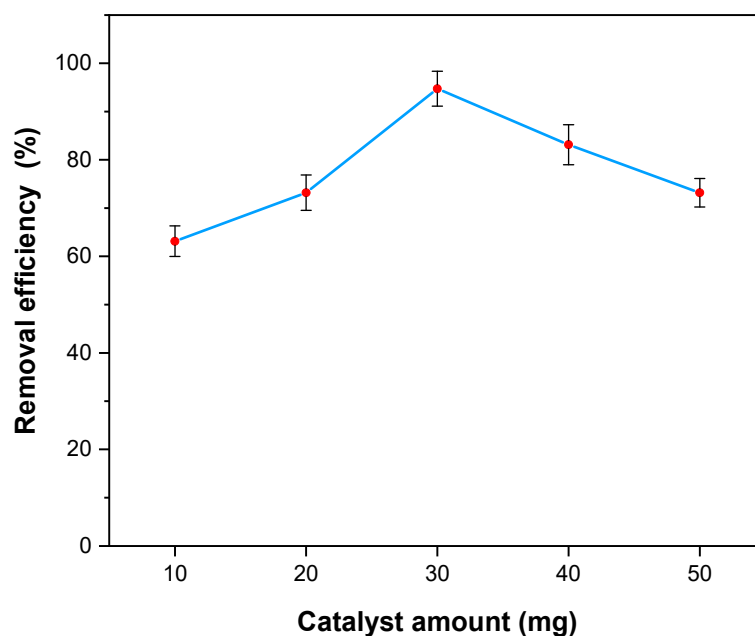


Figure 10. Effect of photocatalyst amount on the photocatalytic removal of MB with B-ZnO/TiO₂ (initial MB concentration: 15 mg/L; photocatalyst amount: 10–50 mg; pH: 11; irradiation time: 15 min).

2.13. Effect of Initial MB Dye Concentration

The initial MB dye solution concentrations varying from 5 to 25 mg/L were used at an optimum photocatalyst amount of 30 mg and pH of 11 to study the effect on the removal efficiency (Figure 11). When the concentration of MB gradually increased from 5 to 25 mg/L, the removal efficiency gradually declined from 98.75% to 70.46%. Additionally, the amount of dye removed increases as the initial dye concentration increases. A steeper slope can be seen between 5 and 15 mg/L, and the slope then gradually flattens off up to 25 mg/L. This phenomenon can be explained as occurring when, at higher dye concentrations, the number of active radicals present in a sample becomes insufficient for the degradation of a higher number of dye molecules. Additionally, when the number of

molecules increases, light penetration is impeded, and prior to reaching the catalyst active surface, photons are interrupted, reducing photocatalytic removal efficiency. Moreover, as the initial concentration of MB is increased, more intermediates are produced, which become adsorbed on the catalyst's active surface. This interrupts the formation of active radicals and decreases the number of active sites available in the photocatalyst [7,11,40]. Due to the concentration of real textile wastewater, 15 mg/L of MB solution was used for the following experiment to investigate the dye removal efficiency.

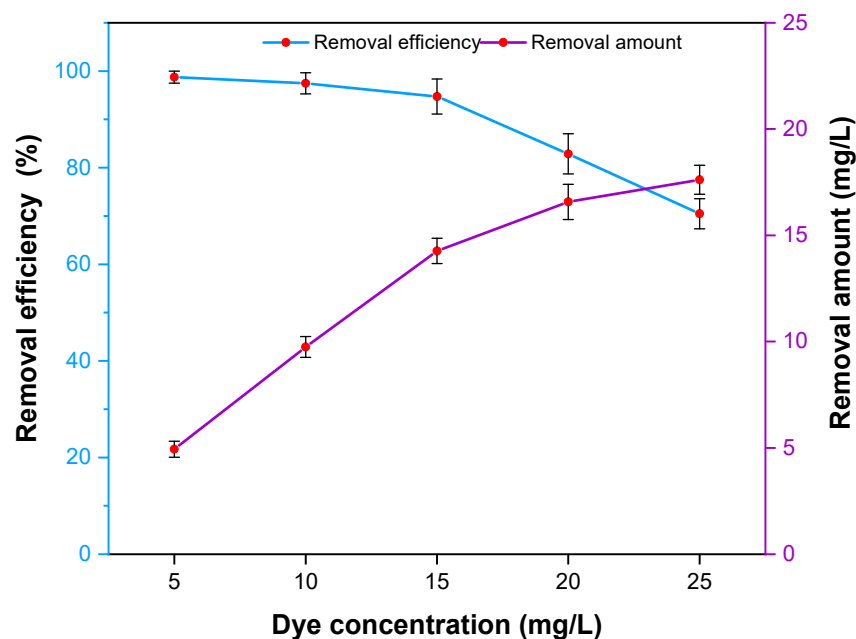


Figure 11. Effect of initial dye concentration on the photocatalytic removal of MB with B–ZnO/TiO₂ (initial MB concentration: 5–25 mg/L; photocatalyst amount: 30 mg; pH: 11; irradiation time: 15 min).

2.14. Effect of Irradiation Time

Figure 12 shows MB removal efficiency using B–ZnO/TiO₂ photocatalyst at different irradiation times (5–25 min) under sunlight irradiation. MB removal efficiency increased when increasing the irradiation time. Almost complete degradation occurs within 25 min of irradiation time. About 54.46% of the dye was removed within 5 min, whereas the MB removal efficiency was 94.73% for 15 min of irradiation. After that, up to 25 min, dye removal efficiency increased slightly as the available dye molecules remaining in the solution were reduced [50].

2.15. Role of Radical Scavengers

To understand the reactive species involved in the B–ZnO/TiO₂ photocatalytic degradation process, scavenger studies were carried out under optimized conditions. Three different chemical scavengers, namely ascorbic acid, 2-propanol, and ammonium oxalate were employed to understand the roles of superoxide radical ions ($\bullet\text{O}_2^-$), hydroxyl radicals ($\bullet\text{OH}$), and photogenerated holes (h^+), respectively [7,50,51]. The photocatalyst was added to the MB solution after the scavengers. The removal efficiency of MB obtained with radical scavengers and B–ZnO/TiO₂ photocatalyst is illustrated in Figure 13. With the introduction of the various scavengers, it was discovered that MB dye removal efficiency was decreased to varying extents. Without any scavenging agent, higher removal efficiency of 94.73% is found for the B–ZnO/TiO₂ photocatalyst. On the other hand, with the addition of ascorbic acid, 2-propanol, and ammonium oxalate, dye removal efficiency is reduced to 61.27%, 60.26%, and 85.29%, respectively. The inhibition of active radicals by various scavengers has led to a significant reduction in the degradation of MB dye [7]. Even though all the radicals were involved in the degradation of the MB dye, the important roles in the photocatalytic

degradation of MB were played by the $\bullet\text{OH}$ and $\bullet\text{O}_2^-$ radicals rather than the h^+ radical under sunlight.

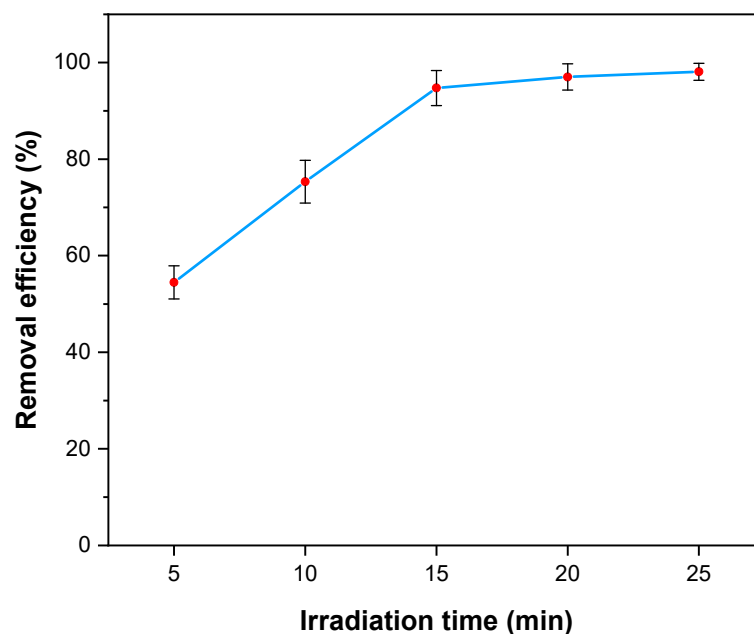


Figure 12. Effect of time on the photocatalytic removal of MB with B-ZnO/TiO₂ (initial MB concentration: 15 mg/L; photocatalyst amount: 30 mg; pH: 11; irradiation time: 5–25 min).

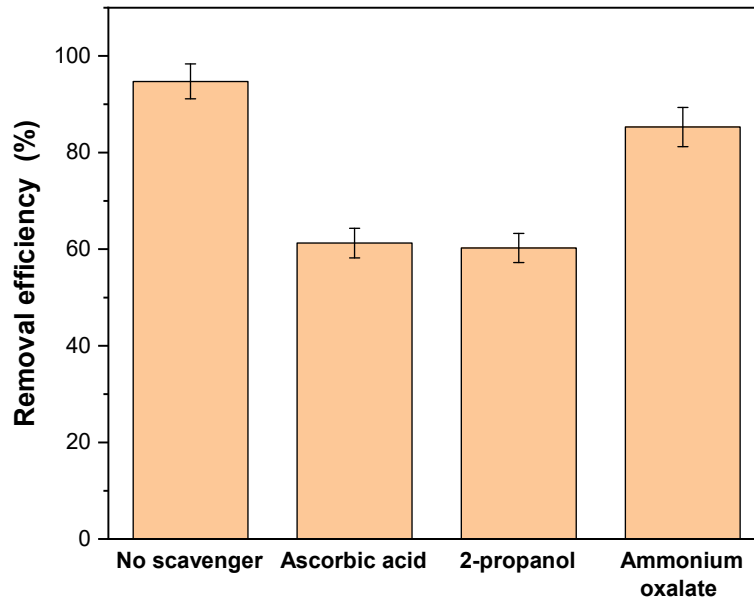


Figure 13. Role of radical scavengers in the photocatalytic removal of MB with B-ZnO/TiO₂ (initial MB concentration: 15 mg/L; concentration of all scavengers: 1 mmol/L; photocatalyst amount: 30 mg; pH: 11; irradiation time: 15 min).

2.16. Photocatalytic Degradation Mechanism

The following Equations (3) and (4) were used to compute the conduction band (CB) and valence band (VB) of ZnO and TiO₂ [35].

$$E_{\text{CB}} = \chi - E_{\text{C}} - 0.5E_{\text{g}} \quad (3)$$

$$E_{\text{VB}} = \chi - E_{\text{C}} + 0.5E_{\text{g}} \quad (4)$$

where E_{CB} and E_{VB} are the CB and VB edge potentials, respectively, and E_g is the bandgap energy of ZnO (~ 2.89 eV) and TiO₂ (~ 3.06 eV). χ represents the electronegativity of ZnO (5.79 eV) and TiO₂ (5.89 eV), while E_C is the energy of free electron on the normal hydrogen electrode scale (4.5 eV) [52,53]. The calculated CB and VB band edge potentials for ZnO are -0.16 and 2.73 eV, respectively, while the edge potentials for TiO₂ are -0.14 and 2.92 eV. Figure 14 schematically depicts the photocatalytic breakdown of MB by B-ZnO/TiO₂ nanocomposites. Electrons (e^-) and holes (h^+) are created from the VB to the CB of ZnO and TiO₂, respectively, when exposed to sunlight. The ECB value of ZnO (-0.16 eV) is more negative than that of TiO₂ (-0.14 eV). As a result, a minor amount of e^- migrates from the CB of ZnO to the CB of TiO₂, while h^+ moves from the VB of TiO₂ to the VB of ZnO, enhancing charge separation [54]. The oxygen (O₂) and water (H₂O) in MB aqueous media can be changed to superoxide ($\bullet O_2^-$) and hydroxyl ($\bullet OH$) radicals by e^- and h^+ , respectively [55]. Scavenger studies also confirm that the $\bullet O_2^-$ and $\bullet OH$ radicals are the most active species for photocatalytic degradation of MB molecules. Due to high oxidation properties, $\bullet O_2^-$ and $\bullet OH$ radicals can react with MB dye and produce CO₂, H₂O, and other nontoxic products [23]. The MB photocatalytic mechanism of B-ZnO/TiO₂ nanocomposites is expressed as follows in Equations (6)–(11) [33,50,56]:

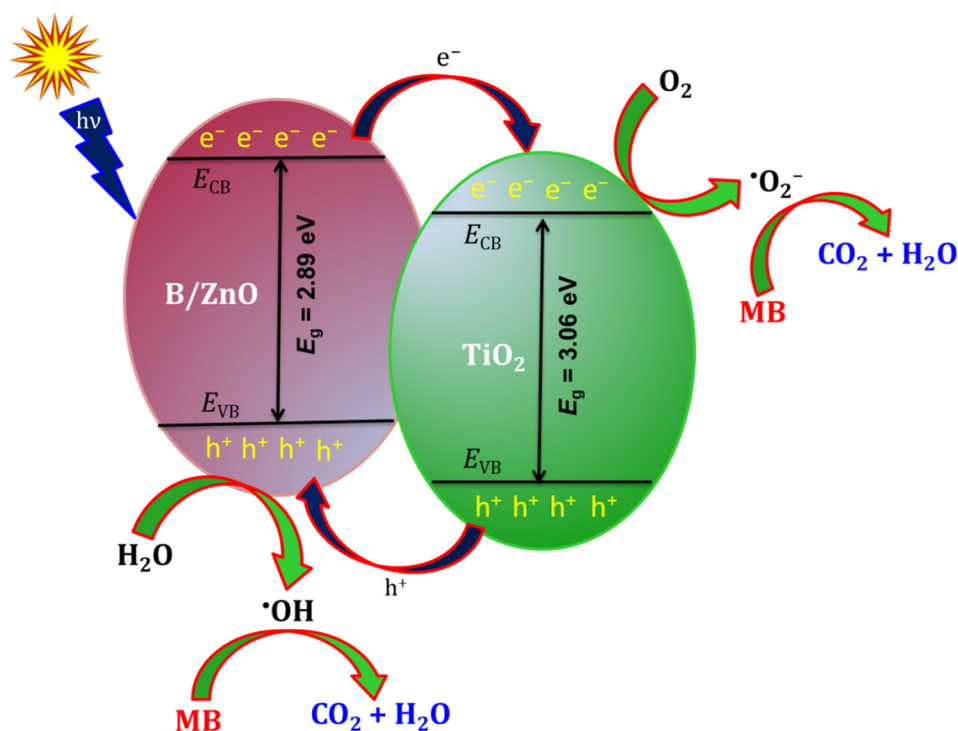
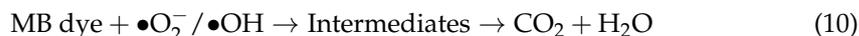
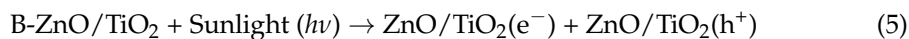


Figure 14. Schematic diagram of B-ZnO/TiO₂ photocatalytic degradation mechanism.

2.17. Photocatalyst Reusability

The reusability of the used B-ZnO/TiO₂ photocatalyst was investigated up to five cycles at the optimal conditions (initial MB concentration: 15 mg/L; photocatalyst amount:

30 mg; pH: 11; irradiation time: 15 min), and the result of the reusability experiments is illustrated in Figure 15. For this purpose, the used photocatalyst was collected and dried for the next cycle [35]. It was found that the MB removal efficiency was marginally decreased for the B–ZnO/TiO₂ photocatalyst in the successive cycles. Because of the poisoning effect of degradation products and the blockage of sunlight irradiation, the dye removal efficiency gradually declined through five cycles [50]. Hence, it can be inferred that B–ZnO/TiO₂ is appropriate for the removal of dye from textile wastewater over a long time and with repeated application.

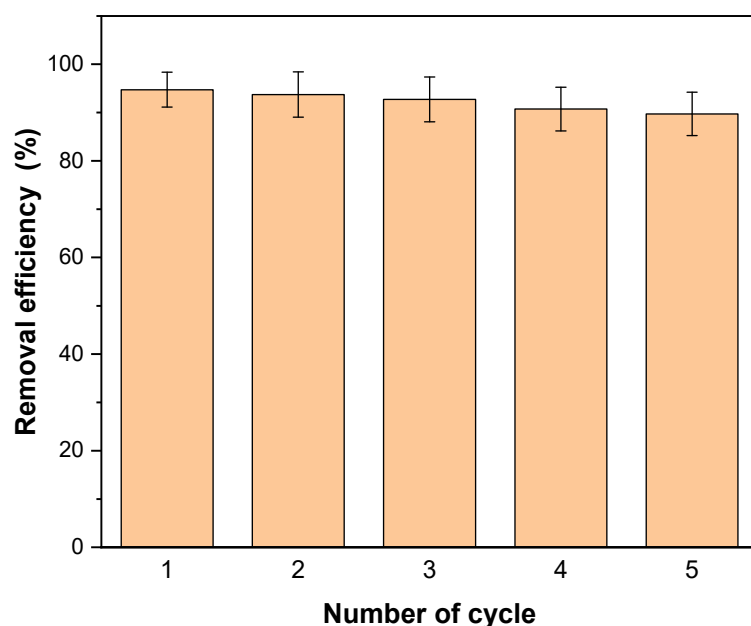


Figure 15. The cycles of photocatalytic experiment of B–ZnO/TiO₂ after five cycles (initial MB concentration: 15 mg/L; photocatalyst amount: 30 mg; pH: 11; irradiation time: 15 min).

3. Materials and Methods

3.1. Materials

Zinc acetate dihydrate (Zn(CH₃COO)₂·2H₂O), oxalic acid dihydrate ((COOH)₂·2H₂O), boric acid (H₃BO₃), commercial TiO₂, methylene blue (C₁₆H₁₈ClN₃S), ascorbic acid (C₆H₈O₆), ammonium oxalate ((NH₄)₂C₂O₄), and 2-propanol ((CH₃)₂CHOH) were obtained from Merck (Darmstadt, Germany). Purified sodium hydroxide (NaOH) pellets and hydrochloric acid (HCl, 37%) were obtained from Active Fine Chemicals Limited (Dhaka, Bangladesh). All the chemicals were analytical grade and were not purified before use. For the preparation of solutions, deionized water was used.

3.2. Synthesis of B–ZnO/TiO₂

B–ZnO/TiO₂ composites were synthesized using a mechanochemical–calcination method with a controlled combustion method. Figure S4 represents the synthesis process used for the fabrication of B–ZnO/TiO₂. For this experiment, the mixture of zinc acetate dihydrate (2.195 g) and oxalic acid dihydrate (2.521 g) was ground for 10 min in an agate mortar to form a paste of zinc oxalate and acetic acid. To obtain the precursor of B–ZnO/TiO₂ (5 wt% B doped with molar ratio 1:1.4 of ZnO/TiO₂), boric acid and commercial TiO₂ were introduced to the above paste, followed by grinding after each addition. The precursor was calcined for 3 h at 500 °C in an air atmosphere to prepare the B–ZnO/TiO₂ composites [57]. For comparison, ZnO, B–ZnO, and ZnO/TiO₂ were also synthesized with the use of the same conditions and without/with the respective additions of boric acid and commercial TiO₂.

3.3. Characterization

An X-ray diffractometer (Ultima IV, Rigaku Corporation, Akishima, Japan) equipped with Cu K α radiation ($\lambda = 0.154$ nm) was used to evaluate the XRD patterns of the samples at room temperature. The XRD data were measured over a scanning range of 10–70° (2θ). The machine was maintained at 40 mA and 40 kV. The scanning step size was 0.02° and the scanning speed was 3° min⁻¹. The surface morphology and particle size distribution of the samples were analyzed by an analytical field emission scanning electron microscope (FESEM, JSM 7600F, JEOL, Japan) equipped with EDS to determine the elemental composition. For FESEM measurements, the accelerating voltage was 5.0 kV, and for EDS analysis, the accelerating voltage was 10 kV. For the identification of the functional groups present in the samples, a Fourier transform infrared spectrometer (FTIR, FT-IR 8400S spectrophotometer (Shimadzu Corporation, Kyoto, Japan)) was used (in the wavenumber range of 4000–400 cm⁻¹; resolution: 4 cm⁻¹; scans: 30). The diffuse reflectance spectra (DRS) of the photocatalysts in the range of 300–700 nm were recorded with a UV-3600i Plus UV-Vis-NIR spectrophotometer (Shimadzu Corporation, Japan). The textural properties of the adsorbents were characterized by nitrogen adsorption–desorption at –196 °C after evacuation for 12 h at 110 °C using a surface area and porosity analyzer (BET Sorptometer, BET-201-A, PMI, Tampa, FL, USA). According to the Brunauer–Emmett–Teller (BET) equation, the surface areas of the photocatalysts were calculated. Photoluminescence (PL) spectra were recorded using a Shimadzu RF-6000 system (Shimadzu Corporation, Kyoto, Japan) equipped with a 150 W xenon lamp at room temperature. The excitation wavelength for each sample was 325 nm, and the emission wavelengths ranged from 200 to 800 nm. X-ray photoelectron spectroscopy (XPS) measurements were carried out with a Thermo Scientific photoelectron spectrometer using Al K α (monochromatic, 1486.6 eV) radiation (UK).

3.4. Removal of MB

The dye removal performance of commercial TiO₂, ZnO, B–ZnO, ZnO/TiO₂, and B–ZnO/TiO₂ photocatalysts was assessed at different operating conditions, including the pH, photocatalyst amount, and initial dye concentration, employing a standard solution of MB ($\lambda_{\text{max}} = 662$ nm [11]) under solar irradiation in open air. Typically, 50 mL of standard MB solution was added to a 250 mL beaker along with 30 mg of synthesized photocatalyst, as illustrated in Figure S5. After exposing the suspensions in the beaker to sunlight, approximately 3 mL of MB solution was collected and filtered using an Advantec membrane filter of 0.45 μm at various time intervals. The remaining concentration of MB after degradation at various conditions was determined by recording absorbance on a UV-1700 Spectrophotometer (Shimadzu, Japan). Batch experiments were conducted under identical conditions (location coordinates: 23.7275° N, 90.4019° E; temperature: ~30 °C; time of year: October to November) on sunny days between 11:00 and 14:00 BST (Bangladesh standard time) for the determination of the percentage removal of MB using the studied photocatalysts. A UV radiometer (UVR-400, Iuchi Co., Osaka, Japan) with a 320–420 nm wavelength sensor was used to measure the intensity of light, as presented in Table S2. To modify the pH of the solutions prior to degradation experiments, aqueous solutions of dilute HCl (0.1 M) and NaOH (0.1 M) were utilized. It is noted that the natural solution pH of MB was ~6.0 [5]. In reusability studies, the catalyst was filtered after each cycle and a fresh MB solution with the same concentration was used. The following equation was used to determine the MB removal efficiency:

$$\text{MB removal efficiency (\%)} = \frac{C - C_0}{C} \times 100 \quad (11)$$

Here, C and C_0 denote the initial and final MB concentrations. All of the experiments were conducted in triplicate, and the results were presented as mean values. The relative standard deviations ranged from 2.5% to 12%.

4. Conclusions

An unprecedented B–ZnO/TiO₂ nanophotocatalyst was synthesized by the mechanochemical–calcination method. Because of the synergistic effects of boron, ZnO, and TiO₂, this catalyst exhibits superior properties and capabilities towards the completion of photocatalytic removal of toxic textile dyes. The synthesized photocatalyst exhibits a crystallite size of 42.54 nm, a BET surface area of 18.99 m²/g, and bandgap energies of 2.89 eV (direct transitions) and 3.06 eV (indirect transitions). The noteworthy reduction in bandgap energy influenced the extension of optical absorption towards the visible-light region, and significant PL quenching in the B–ZnO/TiO₂ photocatalyst spectrum confirmed the reduction in electron–hole recombination rate, which amends the shortcoming of TiO₂ and ZnO. Hence, the B–ZnO/TiO₂ photocatalyst demonstrates better photocatalytic activity, and the MB photocatalytic removal efficiency of ~95% is observed within 15 min of natural sunlight irradiation. The scavenger test was used to determine the probable mechanism of photocatalytic degradation of MB by B–ZnO/TiO₂. The photocatalyst is stable for up to five cycles. Therefore, the synthesized B–ZnO/TiO₂ photocatalyst could be a potential alternative for removing hazardous textile dyes.

Supplementary Materials: The following supporting information can be downloaded at: <https://www.mdpi.com/article/10.3390/catal12030308/s1>, Figure S1: Particle size distribution histograms of (a) commercial TiO₂, (b) ZnO, and (c) B–ZnO/TiO₂, Figure S2: (a) SEM image of B–ZnO/TiO₂ and EDS elemental mapping of (b) boron (B), (c) zinc (Zn), (d) titanium (Ti), and (e) oxygen (O), Figure S3: EDS pattern of (a) commercial TiO₂, (b) ZnO, (c) B–ZnO, (d) ZnO/TiO₂, and (e) B–ZnO/TiO₂, Figure S4: Schematic representation of the synthesis process of B–ZnO/TiO₂, Figure S5: Schematic diagram of the reactor for photocatalytic degradation of MB dye, Table S1: Elemental analysis of commercial TiO₂, ZnO, B–ZnO, ZnO/TiO₂, and B–ZnO/TiO₂ from EDS, Table S2: Sunlight intensity during different experiments.

Author Contributions: Conceptualization, M.A.I.M.; methodology, R.A.S. and M.A.I.M.; software, R.A.S. and M.S.Q.; validation, R.A.S. and M.S.Q.; formal analysis, S.A.F., M.S. and M.A.I.M.; investigation, R.A.S.; resources, M.M., S.M.M. and M.A.I.M.; data curation, M.S.Q. and M.M.; writing—original draft preparation, R.A.S. and M.A.I.M.; writing—review and editing, R.A.S., S.A.F. and M.A.I.M.; visualization, S.A.F., M.S. and S.M.M.; supervision, S.M.M. and M.A.I.M.; project administration, S.M.M. and M.A.I.M.; funding acquisition, S.M.M. and M.A.I.M. All authors have read and agreed to the published version of the manuscript.

Funding: This research was funded by the Centennial Research Grant (CRG) from the University of Dhaka, Bangladesh (Ref. No. Reg/Admin-3/13999).

Data Availability Statement: Data are contained within the article and Supplementary Materials.

Acknowledgments: The authors are grateful to the University of Dhaka, Bangladesh for financial support. We are thankful to the Centre for Advanced Research in Sciences (CARS), University of Dhaka, Bangladesh, the Department of Physics at Bangladesh University of Engineering and Technology (BUET), Dhaka, Bangladesh, and the Bangladesh Council of Scientific and Industrial Research (BCSIR), Dhaka, Bangladesh, for providing partial analytical support to carry out this research.

Conflicts of Interest: The authors declare no conflict of interest. The funders had no role in the design of the study; in the collection, analyses, or interpretation of data; in the writing of the manuscript; or in the decision to publish the results.

References

1. Bayomie, O.S.; Kandeel, H.; Shoeib, T.; Yang, H.; Youssef, N.; El-Sayed, M.M.H. Novel approach for effective removal of methylene blue dye from water using fava bean peel waste. *Sci. Rep.* **2020**, *10*, 7824. [[CrossRef](#)] [[PubMed](#)]
2. Houas, A.; Lachheb, H.; Ksibi, M.; Elaloui, E.; Guillard, C.; Herrmann, J.M. Photocatalytic degradation pathway of methylene blue in water. *Appl. Catal. B Environ.* **2001**, *31*, 145–157. [[CrossRef](#)]
3. Chen, D.; Cheng, Y.; Zhou, N.; Chen, P.; Wang, Y.; Li, K.; Huo, S.; Cheng, P.; Peng, P.; Zhang, R.; et al. Photocatalytic degradation of organic pollutants using TiO₂-based photocatalysts: A review. *J. Clean. Prod.* **2020**, *268*, 121725. [[CrossRef](#)]
4. Gnanaprakasam, A.; Sivakumar, V.M.; Thirumarimurugan, M. Influencing Parameters in the Photocatalytic Degradation of Organic Effluent via Nanometal Oxide Catalyst: A Review. *Indian J. Mater. Sci.* **2015**, *2015*, 1–16. [[CrossRef](#)]

5. Azeez, F.; Al-Hetlani, E.; Arafa, M.; Abdelmonem, Y.; Nazeer, A.A.; Amin, M.O.; Madkour, M. The effect of surface charge on photocatalytic degradation of methylene blue dye using chargeable titania nanoparticles. *Sci. Rep.* **2018**, *8*, 7104. [[CrossRef](#)] [[PubMed](#)]
6. Ameta, R.; Benjamin, S.; Ameta, A.; Ameta, S.C. Photocatalytic degradation of organic pollutants: A review. *Mater. Sci. Forum* **2013**, *734*, 247–272. [[CrossRef](#)]
7. Gupta, D.; Chauhan, R.; Kumar, N.; Singh, V.; Srivastava, V.C.; Mohanty, P.; Mandal, T.K. Enhancing photocatalytic degradation of quinoline by ZnO:TiO₂ mixed oxide: Optimization of operating parameters and mechanistic study. *J. Environ. Manag.* **2020**, *258*, 110032. [[CrossRef](#)]
8. Mohtar, S.S.; Aziz, F.; Ismail, A.F.; Sambudi, N.S.; Abdullah, H.; Rosli, A.N.; Ohtani, B. Impact of doping and additive applications on photocatalyst textural properties in removing organic pollutants: A review. *Catalysts* **2021**, *11*, 1160. [[CrossRef](#)]
9. Mulpuri, R.K.; Tirukkavalluri, S.R.; Imandi, M.R.; Alim, S.A.; Lakshmi Kapuganti, V.D. Zinc and boron co-doped nanotitania with enhanced photocatalytic degradation of acid red 6A under visible light irradiation. *Sustain. Environ. Res.* **2019**, *1*, 29.
10. Giahhi, M.; Saadat Niavol, S.; Taghavi, H.; Meskinfam, M. Synthesis and characterization of ZnO-TiO₂ nanopowders doped with Fe via sol-gel method and their application in photocatalytic degradation of anionic surfactant. *Russ. J. Phys. Chem. A* **2015**, *89*, 2432–2437. [[CrossRef](#)]
11. Sakib, A.A.M.; Masum, S.M.; Hoinkis, J.; Islam, R.; Molla, M.A.I. Synthesis of CuO/ZnO Nanocomposites and Their Application in Photodegradation of Toxic Textile Dye. *J. Compos. Sci.* **2019**, *3*, 91. [[CrossRef](#)]
12. Wu, Y.; Gong, Y.; Liu, J.; Zhang, Z.; Xu, Y.; Ren, H.; Li, C.; Niu, L. B and Y co-doped TiO₂ photocatalyst with enhanced photodegradation efficiency. *J. Alloys Compd.* **2017**, *695*, 1462–1469. [[CrossRef](#)]
13. Wetchakun, K.; Wetchakun, N.; Sakulsermsuk, S. An overview of solar/visible light-driven heterogeneous photocatalysis for water purification: TiO₂- and ZnO-based photocatalysts used in suspension photoreactors. *J. Ind. Eng. Chem.* **2019**, *71*, 19–49. [[CrossRef](#)]
14. Islam, M.M.; Ahmed, A.Z.; Kabir, S.F.; Islam, R.; Islam Molla, M.A. Optimization of Photodegradation Conditions of Rhodamine B in Water with Dye-Sensitized Titanium Dioxide. *J. CleanWAS* **2020**, *4*, 28–31. [[CrossRef](#)]
15. Liu, C.; Li, X.; Xu, C.; Wu, Y.; Hu, X.; Hou, X. Boron-doped rutile TiO₂/anatase TiO₂/ZrTiO₄ ternary heterojunction photocatalyst with optimized phase interface and band structure. *Ceram. Int.* **2020**, *46*, 20943–20953. [[CrossRef](#)]
16. Niu, P.; Wu, G.; Chen, P.; Zheng, H.; Cao, Q.; Jiang, H. Optimization of Boron Doped TiO₂ as an Efficient Visible Light-Driven Photocatalyst for Organic Dye Degradation with High Reusability. *Front. Chem.* **2020**, *8*, 1–8. [[CrossRef](#)]
17. Panwar, S.; Upadhyay, G.K.; Purohit, L.P. Gd-doped ZnO:TiO₂ heterogenous nanocomposites for advance oxidation process. *Mater. Res. Bull.* **2022**, *145*, 111534. [[CrossRef](#)]
18. Kerli, S.; Kavgaci, M.; Soğuksu, A.K.; Avar, B. Photocatalytic Degradation of Methylene Blue, Rhodamine-B, and Malachite Green by Ag @ ZnO/TiO₂. *Braz. J. Phys.* **2021**, *52*, 22. [[CrossRef](#)]
19. Li, W.; Wu, D.; Yu, Y.; Zhang, P.; Yuan, J.; Cao, Y.; Cao, Y.; Xu, J. Investigation on a novel ZnO/TiO₂-B photocatalyst with enhanced visible photocatalytic activity. *Phys. E Low-Dimens. Syst. Nanostruct.* **2014**, *58*, 118–123. [[CrossRef](#)]
20. Wang, Y.; Liu, X.; Guo, L.; Shang, L.; Ge, S.; Song, G.; Naik, N.; Shao, Q.; Lin, J.; Guo, Z. Metal organic framework-derived C-doped ZnO/TiO₂ nanocomposite catalysts for enhanced photodegradation of Rhodamine B. *J. Colloid Interface Sci.* **2021**, *599*, 566–576. [[CrossRef](#)]
21. Munguti, L.; Dejene, F. Influence of annealing temperature on structural, optical and photocatalytic properties of ZnO-TiO₂ composites for application in dye removal in water. *Nano Struct. Nano Objects* **2020**, *24*, 100594. [[CrossRef](#)]
22. Teh, C.M.; Mohamed, A.R. Roles of titanium dioxide and ion-doped titanium dioxide on photocatalytic degradation of organic pollutants (phenolic compounds and dyes) in aqueous solutions: A review. *J. Alloys Compd.* **2011**, *509*, 1648–1660. [[CrossRef](#)]
23. Ahmed, A.Z.; Islam, M.M.; Islam, M.M.u.; Masum, S.M.; Islam, R.; Molla, M.A.I. Fabrication and characterization of B/Sn-doped ZnO nanoparticles via mechanochemical method for photocatalytic degradation of rhodamine B. *Inorg. Nano-Metal Chem.* **2020**, *51*, 1369–1378. [[CrossRef](#)]
24. Kumar, S.; Maivizhikannan, V.; Drews, J.; Krishnan, V. Fabrication of nanoheterostructures of boron doped ZnO-MoS₂ with enhanced photostability and photocatalytic activity for environmental remediation applications. *Vacuum* **2019**, *163*, 88–98. [[CrossRef](#)]
25. Molla, M.A.I.; Furukawa, M.; Tateishi, I.; Katsumata, H.; Suzuki, T.; Kaneco, S. Photocatalytic Decolorization of Dye with Self-Dye-Sensitization under Fluorescent Light Irradiation. *ChemEngineering* **2017**, *1*, 8. [[CrossRef](#)]
26. Mousa, H.M.; Alenezi, J.F.; Mohamed, I.M.A.; Yasin, A.S.; Hashem, A.F.M.; Abdal-hay, A. Synthesis of TiO₂@ZnO heterojunction for dye photodegradation and wastewater treatment. *J. Alloys Compd.* **2021**, *886*, 161169. [[CrossRef](#)]
27. Gohari, G.; Mohammadi, A.; Akbari, A.; Panahirad, S.; Dadpour, M.R.; Fotopoulos, V.; Kimura, S. Titanium dioxide nanoparticles (TiO₂ NPs) promote growth and ameliorate salinity stress effects on essential oil profile and biochemical attributes of *Dracocephalum moldavica*. *Sci. Rep.* **2020**, *10*, 912. [[CrossRef](#)]
28. Ismail, M.A.; Taha, K.K.; Modwi, A.; Khezami, L. ZnO nanoparticles: Surface and X-ray profile analysis. *J. Ovonic Res.* **2018**, *14*, 381–393.
29. Wang, W.; Ai, T.; Yu, Q. Electrical and photocatalytic properties of boron-doped ZnO nanostructure grown on PET-ITO flexible substrates by hydrothermal method. *Sci. Rep.* **2017**, *7*, 42615. [[CrossRef](#)]

30. Wolfgong, W.J. Chemical analysis techniques for failure analysis: Part 1, common instrumental methods. In *Handbook of Materials Failure Analysis with Case Studies from the Aerospace and Automotive Industries*; Butterworth-Heinemann: Oxford, UK, 2016; pp. 279–307.
31. El Mragui, A.; Daou, I.; Zegaoui, O. Influence of the preparation method and ZnO/(ZnO + TiO₂) weight ratio on the physico-chemical and photocatalytic properties of ZnO-TiO₂ nanomaterials. *Catal. Today* **2018**, *321–322*, 41–51. [[CrossRef](#)]
32. Shaikh, S.F.; Mane, R.S.; Min, B.K.; Hwang, Y.J.; Joo, O.S. D-sorbitol-induced phase control of TiO₂ nanoparticles and its application for dye-sensitized solar cells. *Sci. Rep.* **2016**, *6*, 20103. [[CrossRef](#)]
33. Ebraheem, S.; El-Saied, A. Band Gap Determination from Diffuse Reflectance Measurements of Irradiated Lead Borate Glass System Doped with TiO₂ by Using Diffuse Reflectance Technique. *Mater. Sci. Appl.* **2013**, *4*, 324–329.
34. Tekin, D.; Kiziltas, H.; Urgan, H. Kinetic evaluation of ZnO/TiO₂ thin film photocatalyst in photocatalytic degradation of Orange G. *J. Mol. Liq.* **2020**, *306*, 112905. [[CrossRef](#)]
35. Molla, M.A.I.; Furukawa, M.; Tateishi, I.; Katsumata, H.; Kaneco, S. Fabrication of Ag-doped ZnO by mechanochemical combustion method and their application into photocatalytic Famotidine degradation. *J. Environ. Sci. Heal. Part A Toxic Hazard. Subst. Environ. Eng.* **2019**, *54*, 914–923. [[CrossRef](#)]
36. Sultana, F.; Dey, S.C.; Molla, M.A.I.; Hossain, M.R.; Rahman, M.M.; Quddus, M.S.; Moniruzzaman, M.; Shamsuddin, S.M.; Sarker, M. Facile synthesis of TiO₂/Chitosan nanohybrid for adsorption-assisted rapid photodegradation of an azo dye in water. *React. Kinet. Mech. Catal.* **2021**, *133*, 1121–1139. [[CrossRef](#)]
37. Yadav, K.; Gahlaut, S.K.; Mehta, B.R.; Singh, J.P. Photoluminescence based H₂ and O₂ gas sensing by ZnO nanowires. *Appl. Phys. Lett.* **2016**, *108*, 071602. [[CrossRef](#)]
38. Alamdari, S.; Ghamsari, M.S.; Afarideh, H.; Mohammadi, A.; Geranmayeh, S.; Tafreshi, M.J.; Ehsani, M.H. Preparation and characterization of GO-ZnO nanocomposite for UV detection application. *Opt. Mater. Amst.* **2019**, *92*, 243–250. [[CrossRef](#)]
39. Zhang, Q.; Li, C. TiO₂ Coated ZnO Nanorods by Mist Chemical Vapor Deposition for Application as Photoanodes for Dye-Sensitized Solar Cells. *Nanomaterials* **2019**, *9*, 1339. [[CrossRef](#)]
40. Pant, B.; Ojha, G.P.; Kuk, Y.S.; Kwon, O.H.; Wan Park, Y.; Park, M. Synthesis and characterization of ZnO-TiO₂/carbon fiber composite with enhanced photocatalytic properties. *Nanomaterials* **2020**, *10*, 1960. [[CrossRef](#)]
41. Delsouz Khaki, M.R.; Shafeeyan, M.S.; Raman, A.A.A.; Daud, W.M.A.W. Evaluating the efficiency of nano-sized Cu doped TiO₂/ZnO photocatalyst under visible light irradiation. *J. Mol. Liq.* **2018**, *258*, 354–365. [[CrossRef](#)]
42. Guo, J.; Li, J.; Yin, A.; Fan, K.; Dai, W. Photodegradation of Rhodamine B on Sulfur Doped ZnO/TiO₂ Nanocomposite Photocatalyst under Visible-light Irradiation. *Chin. J. Chem.* **2010**, *28*, 2144–2150. [[CrossRef](#)]
43. Zou, X.; Dong, X.; Wang, L.; Ma, H.; Zhang, X.; Zhang, X. Preparation of Ni doped ZnO-TiO₂ composites and their enhanced photocatalytic activity. *Int. J. Photoenergy* **2014**, *2014*, 893158. [[CrossRef](#)]
44. Xie, H.; Ding, F.; Mu, H. Effects of Au nanoparticles and ZnO morphology on the photocatalytic performance of Au doped ZnO/TiO₂ films. *Nanotechnology* **2019**, *30*, 085708. [[CrossRef](#)]
45. Viet, T.Q.Q.; Khoi, V.H.; Thi Huong Giang, N.; Thi Van Anh, H.; Dat, N.M.; Phong, M.T.; Hieu, N.H. Statistical screening and optimization of photocatalytic degradation of methylene blue by ZnO-TiO₂/rGO nanocomposite. *Colloids Surf. A Physicochem. Eng. Asp.* **2021**, *629*, 127464. [[CrossRef](#)]
46. Pal, P. Industry-Specific Water Treatment Case Studies. In *Industrial Water Treatment Process Technology*; Butterworth-Heinemann: Oxford, UK, 2017; pp. 243–511.
47. Molla, M.A.I.; Furukawa, M.; Tateishi, I.; Katsumata, H.; Kaneco, S. Mineralization of Diazinon with nanosized-photocatalyst TiO₂ in water under sunlight irradiation: Optimization of degradation conditions and reaction pathway. *Environ. Technol.* **2020**, *41*, 3524–3533. [[CrossRef](#)]
48. Benhebal, H.; Chaib, M.; Salmon, T.; Geens, J.; Leonard, A.; Lambert, S.D.; Crine, M.; Heinrichs, B. Photocatalytic degradation of phenol and benzoic acid using zinc oxide powders prepared by the sol-gel process. *Alex. Eng. J.* **2013**, *52*, 517–523. [[CrossRef](#)]
49. Molla, M.A.I.; Ahsan, S.; Tateishi, I.; Furukawa, M.; Katsumata, H.; Suzuki, T.; Kaneco, S. Degradation, Kinetics, and Mineralization in Solar Photocatalytic Treatment of Aqueous Amitrole Solution with Titanium Dioxide. *Environ. Eng. Sci.* **2018**, *35*, 401–407. [[CrossRef](#)]
50. Mondol, B.; Sarker, A.; Shareque, A.M.; Dey, S.C.; Islam, M.T.; Das, A.K.; Shamsuddin, S.M.; Molla, M.A.I.; Sarker, M. Preparation of Activated Carbon/TiO₂ Nanohybrids for Photodegradation of Reactive Red-35 Dye Using Sunlight. *Photochem* **2021**, *1*, 54–66. [[CrossRef](#)]
51. Molla, M.A.I.; Tateishi, I.; Furukawa, M.; Katsumata, H.; Suzuki, T.; Kaneco, S. Evaluation of Reaction Mechanism for Photocatalytic Degradation of Dye with Self-Sensitized TiO₂ under Visible Light Irradiation. *Open J. Inorg. Non-Met. Mater.* **2017**, *7*, 1–7.
52. Tian, J.; Shao, Q.; Zhao, J.; Pan, D.; Dong, M.; Jia, C.; Ding, T.; Wu, T.; Guo, Z. Microwave solvothermal carboxymethyl chitosan templated synthesis of TiO₂/ZrO₂ composites toward enhanced photocatalytic degradation of Rhodamine B. *J. Colloid Interface Sci.* **2019**, *541*, 18–29. [[CrossRef](#)]
53. Yu, Z.; Moussa, H.; Liu, M.; Schneider, R.; Moliere, M.; Liao, H. Heterostructured metal oxides-ZnO nanorods films prepared by SPPS route for photodegradation applications. *Surf. Coat. Technol.* **2019**, *375*, 670–680. [[CrossRef](#)]

54. Hou, X.; Stanley, S.L.; Zhao, M.; Zhang, J.; Zhou, H.; Cai, Y.; Huang, F.; Wei, Q. MOF-based C-doped coupled TiO₂/ZnO nanofibrous membrane with crossed network connection for enhanced photocatalytic activity. *J. Alloys Compd.* **2019**, *777*, 982–990. [[CrossRef](#)]
55. Kabir, R.; Saifullah, M.A.K.; Ahmed, A.Z.; Masum, S.M.; Molla, M.A.I. Synthesis of N-Doped ZnO Nanocomposites for Sunlight Photocatalytic Degradation of Textile Dye Pollutants. *J. Compos. Sci.* **2020**, *4*, 49. [[CrossRef](#)]
56. Molla, M.A.I.; Ahmed, A.Z.; Kaneco, S. *Reaction Mechanism for Photocatalytic Degradation of Organic Pollutants*; Elsevier, B.V.: Amsterdam, The Netherlands, 2021; ISBN 9780128230077.
57. Molla, M.A.I.; Furukawa, M.; Tateishi, I.; Katsumata, H.; Kaneco, S. Studies of Effects of Calcination Temperature on the Crystallinity and Optical Properties of Ag-Doped ZnO Nanocomposites. *J. Compos. Sci.* **2019**, *3*, 18. [[CrossRef](#)]